

Elastic microseismic full waveform inversion: synthetic and real data

Nadine Igonin* and Kristopher Innanen*

ABSTRACT

In the microseismic and seismology field, determining the hypocenter of seismic events is necessary, and requires an accurate velocity model. In conventional FWI, one of the outputs is often a P- and/or S-wave velocity model obtained from (in most cases) sources on the surface. It is not difficult to imagine a framework where microseismic events could be used as additional subsurface sources that could increase the illumination in the reservoir. Furthermore, the velocity model obtained from such a scheme would be useful to re-locate said microseismic events more accurately. Therefore, this symbiotic relationship can be taken advantage of to formulate a FWI implementation where microseismic events are used to simultaneously update the velocity model, and the source position. This would involve two updates at each iteration - one for the velocity model and one for the source position. In this report, we explore in detail the source-term gradient in an elastic 2D formulation. We discuss the effect of the starting position, dominant frequency, moment tensor, and receiver geometry. Furthermore, we explore the impact of cross-talk due to having an incorrect starting velocity model. Finally, we end with preliminary results with a real dataset from the Horn River Basin, British Columbia.

INTRODUCTION

Full waveform inversion (FWI) is an inversion scheme that was developed in the 1980's (Tarantola, 1984). The basic premise of the method is to use the difference between the true and modelled data, as well as directionality derived from gradients and the Hessian of the objective function to iteratively update seismic models. Since then, increasingly complex implementations of FWI have been developed, with synthetic examples functioning on elastic, anisotropic models. There have been successful applications of FWI in marine environments, and there are even recent examples of land FWI (Pan, 2018). Multiparameter FWI is also becoming increasingly popular. Common examples include parameterizing in terms of P-wave velocity, S-wave velocity, and density. Recent advances involve also solving for attenuation and anisotropic parameters (Ex. Keating and Innanen (2018)).

The focus of this report is to build on a multiparameter implementation of FWI to microseismic data. The motivation for microseismic FWI (MFWI) is summarized in Figure 1. When working in a certain region, most geophysical applications require a velocity model. This can be obtained as an output from conventional exploration seismic, or from well-log data. Indeed, a velocity model may be obtained from FWI generated from seismic data. If the region of interest is host to seismic activity, be it from hydraulic fracturing, carbon capture and storage, geothermal activity, or even natural seismicity, then this velocity model may be used to locate the events. The goal of MFWI is to take advantage of the reversibility of wavefields, and use the microseismic events as added source illumination in order to

*CREWES - University of Calgary

improve the velocity model. Then, the new velocity model may be used to re-locate the events, and an iterative scheme emerges.

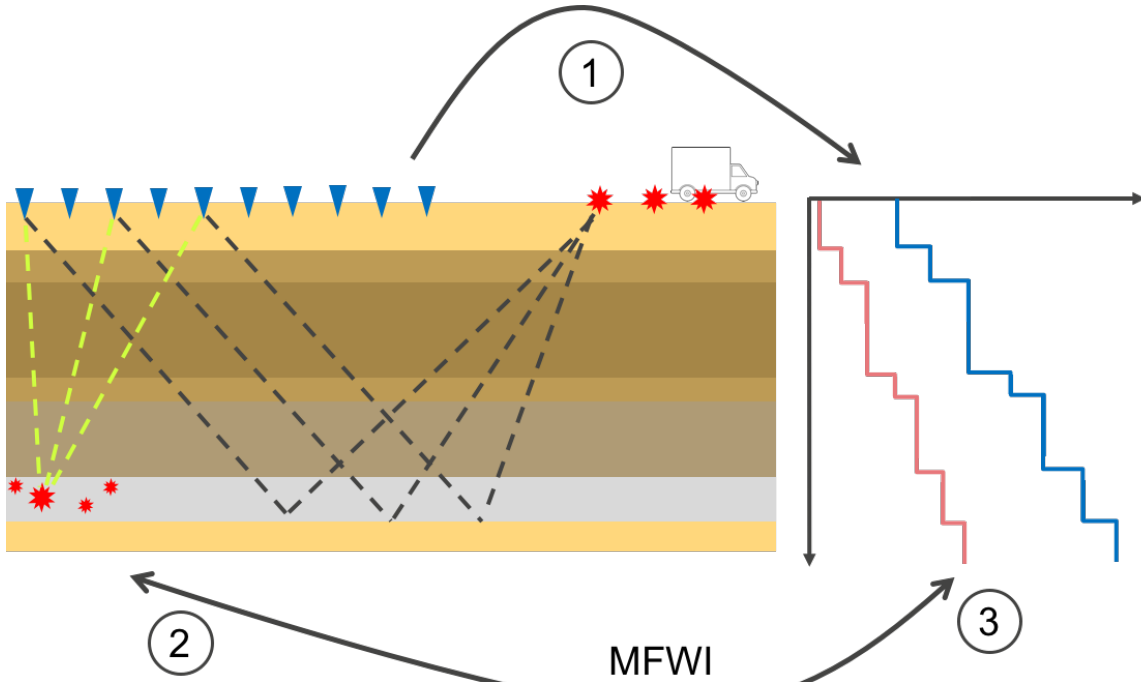


FIG. 1. Concept of microseismic full waveform inversion (MFWI). (1) Seismic exploration or well logging leads to an initial velocity model, which is then (2) used to locate microseismic events. (3) In turn, those microseismic events can be used to refine the velocity model and locations iteratively.

The concept of MFWI was introduced in Igonin and Innanen (2017a), and applied in the acoustic case in Igonin and Innanen (2017b). This preliminary implementation led to many interesting results, among which was the determination of the basic character of the source-term gradient, and a first look at the nature of the cross-talk in this multiparameter problem. This report builds on that knowledge by first expanding to the elastic environment. This invites the exploration of the same questions as the acoustic environment, so the nature of the source-term gradient is revisited. Additionally, due to having both P- and S-waves propagating through the medium, the cross-talk exhibited is more complex, and that is explored herein. Finally, elastic MFWI is applied to a real microseismic dataset.

Recently, there have been a few publications working on applications of FWI with microseismic data. For example, in the last year, one of the notable applications has been by Wang and Alkhalifah (2018), who devised a method to perform FWI with synthetic acoustic 2D microseismic events. Their key contribution was to implement a method that was independent of the source signature, which is often difficult to estimate in real data examples. Other approaches for simultaneous inversion for source position and velocity model involving other types of inversion (not FWI) have also been developed, such as inversion for travel times (Zhang et al., 2018; Tan et al., 2018). However, to date, there have been few applications of elastic MFWI and there are limited results with real data.

ELASTIC MFWI FORMULATION

Given an objective function ϕ , a velocity model \mathbf{s}_c and a source distribution \mathbf{s}_s , the full framework for MFWI is given by

$$\begin{bmatrix} \mathbf{g}_c \\ \mathbf{g}_s \end{bmatrix} = - \begin{bmatrix} \mathbf{H}_{cc} & \mathbf{H}_{cs} \\ \mathbf{H}_{sc} & \mathbf{H}_{ss} \end{bmatrix}^{-1} \begin{bmatrix} \mathbf{g}_c \\ \mathbf{g}_s \end{bmatrix} \quad (1)$$

where

$$\mathbf{g}_s = \frac{\partial \phi}{\partial \mathbf{s}_s} \quad \text{and} \quad \mathbf{g}_c = \frac{\partial \phi}{\partial \mathbf{s}_c} \quad (2)$$

are the gradients with respect to \mathbf{s}_c and \mathbf{s}_s , and the Hessian consists of block matrices of second order partial derivatives of ϕ where the first partial derivative is with respect to the first index and the second partial derivative is with respect to the second index. The objective function in this case is given by

$$\phi = - \sum_{r_g, r_s} \frac{1}{2} \int dt (d(\mathbf{r}_g, \mathbf{r}_s, t) - p(\mathbf{r}_g, \mathbf{r}_s, t | \mathbf{s}_c, \mathbf{s}_s))^2, \quad (3)$$

where \mathbf{r}_g is the receiver position, \mathbf{r}_s is the source position, \mathbf{s}_c is the velocity distribution, \mathbf{s}_s is the source distribution, $d(\dots)$ is the observed data, and $p(\dots)$ is the modelled data. In the previous work on acoustic MFWI (Igonin and Innanen, 2017a,b), the following equation was derived for the time-domain source-term gradient, g_s ,

$$g_s(\mathbf{r}) = - \sum_{r_g, r_s} \int dt \delta P(\mathbf{r}_g, \mathbf{r}_s, t | \mathbf{s}_c, \mathbf{s}_s) g(\mathbf{r}_g, \mathbf{r}, t - t^* | \mathbf{s}_c, \mathbf{s}_s), \quad (4)$$

where $\delta P(\dots)$ is the difference between the observed and modelled wavefields, t^* is the event origin time (assumed to be zero), and $g(\dots)$ is the observed wavefield. The behaviour of this gradient was similar to that of a dipole, with negative values arising at incorrect source locations, and positive values arising at source locations in the correct direction. The elastic environment is more complicated, as it contains both P- and S-wavefields. However, we posit that the form of the source-term gradient would remain the same, and be given by the same formula. The only difference would be that \mathbf{s}_c now refers to the P- and S-wave velocities.

This formulation is geared toward inverting for source position, and does not explicitly state the moment tensor or source wavelet. Therefore, in order to invert for those, or other quantities, a more complex form for the gradient would have to be derived. That remains outside the scope of this report, though the limitations of this current form will be discussed and explored in the following sections.

SYNTHETIC ELASTIC MFWI

A 3D anelastic, anisotropic finite difference code written by Boyd (2006) was used to implement elastic MFWI. This code was modified by Rashedi (2015) to incorporate a moment tensor source and allow for the specification of moment magnitude. In the following sections, the basic behaviour and character of the elastic source-term gradient will be discussed in terms of starting position, frequency, and moment tensor. Finally, the synthetic section will conclude with a first look at the potential cross-talk between the velocity model and source location in the elastic case.

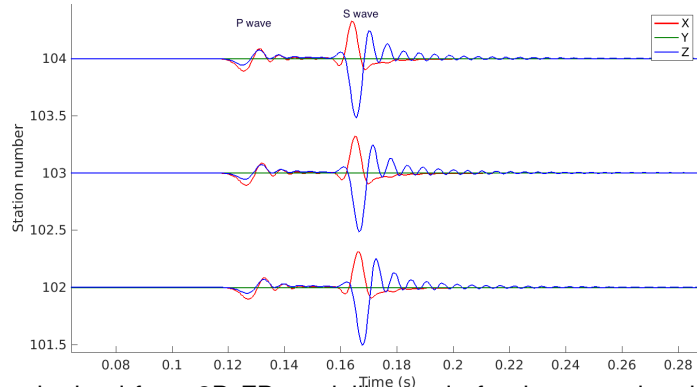


FIG. 2. Waveforms obtained from 2D FD modelling code for three receiver locations. P- and S-waves are labelled.

To begin with, as we can see from Equation 3, the construction of the source-term gradient only requires two terms. Figure 2 shows an example of the waveforms generated from the finite difference code. The waveforms are quite simple, but as a proof of concept for elastic MFWI, they exhibit the features necessary for the analysis (P- and S-wave arrivals, variation in amplitudes depending on moment tensor etc.). In this 2D environment, there are only x and z components of the wavefield, and a choice needed to be made about how to use these two components. Figure 3 shows the gradient created from the z component, the x component, and the sum of the two. The gradient from the z component alone gives an update in the correct direction (see following sections for explanation of how to interpret the gradient figures), whereas the contribution of the x component is less clear. For simplicity, the remainder of this report deals with results that are limited to using only the z component.

In the very first implementation of the algorithm, receivers were placed at all locations of the 2D model to see what the full solution looks like if everything is known. However, even in novel algorithms, in order to test that the method is viable, the largest acceptable extent of the receivers is along the four boundaries. Figure 4 shows a comparison of the gradient with receivers everywhere, and receivers limited to the boundaries. The overall character in both cases is similar, but when the receivers are limited to the sides, the next source position is laterally offset from where it is in Figure 4a. Since the behaviour is still in the overall direction that is useful, we will proceed with this implementation, while also keeping in mind that we would like our gradient to look more like Figure 4a (see Discussion for more on possible regularizations).

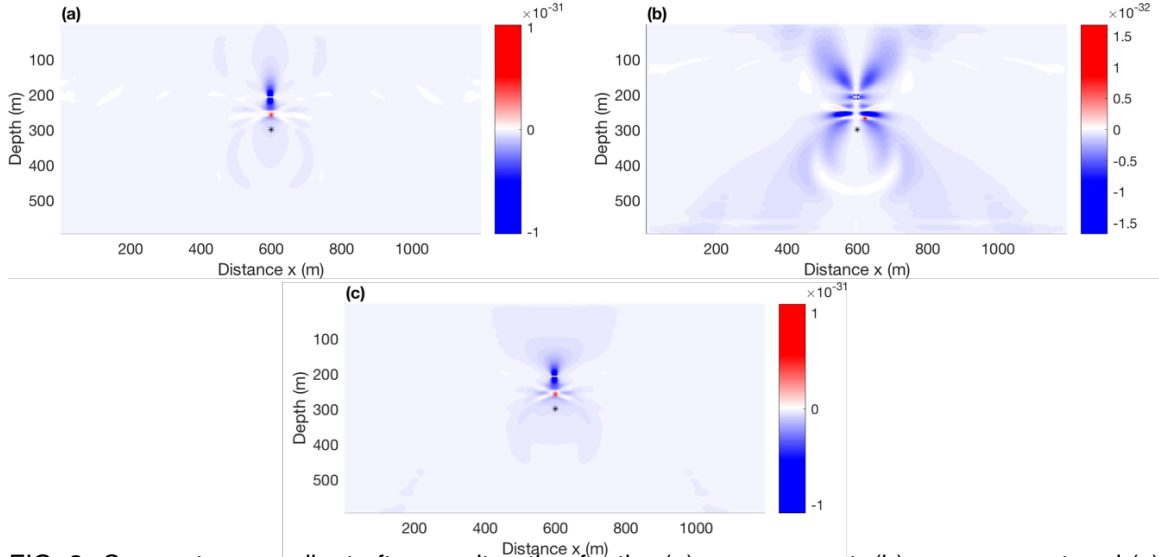


FIG. 3. Source-term gradient after one iteration for the (a) z component, (b) x component and (c) both the x and z components. Red stars indicate the position of the maximum of the gradient, which is taken as the next source position for the subsequent iteration. Black stars indicate the true source position. The starting source position is at the center of each dark blue region.

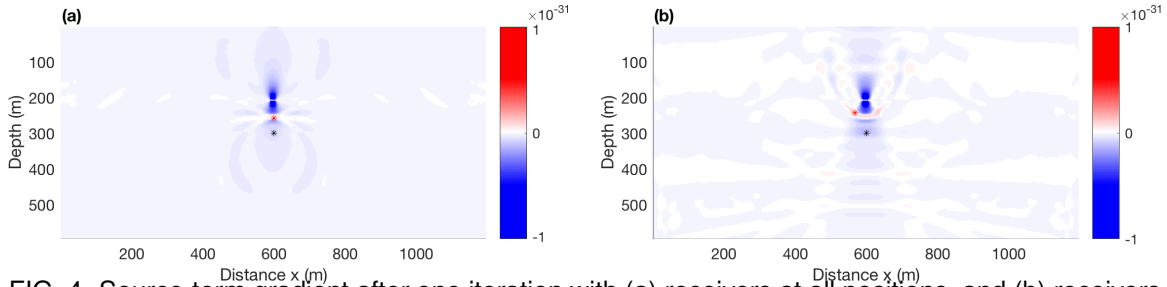


FIG. 4. Source-term gradient after one iteration with (a) receivers at all positions, and (b) receivers only along the four boundaries. Red stars indicate the position of the maximum of the gradient, which is taken as the next source position for the subsequent iteration. Black stars indicate the true source position. The starting source position is at the center of each dark blue region.

Separation distance

In the acoustic implementation, we showed that the separation distance between the starting position and the true source position changes the shape of the gradient. Therefore, the first test is to see if it is the same case in the elastic implementation.

A homogeneous background velocity was defined, and the source was put in the middle of a 400×200 size grid with a spacing of 3 m. For simplicity, a frequency of 30 Hz was chosen, and a double couple moment tensor source (assumed to be known) was used. Figure 5 shows the gradient in the case where the starting position is 30 m, 90 m, and 210 m, respectively.

First, we can remark that the overall appearance of the elastic source-term gradient is quite similar to the acoustic source-term gradient. It has a dipole-like character, with a larger negative lobe at the incorrect position, and a smaller positive lobe in the direction of the correct location. In Figure 5a-c, the basic shape of the gradient does not change, and it maintains its ‘butterfly’ character regardless of the separation distance.

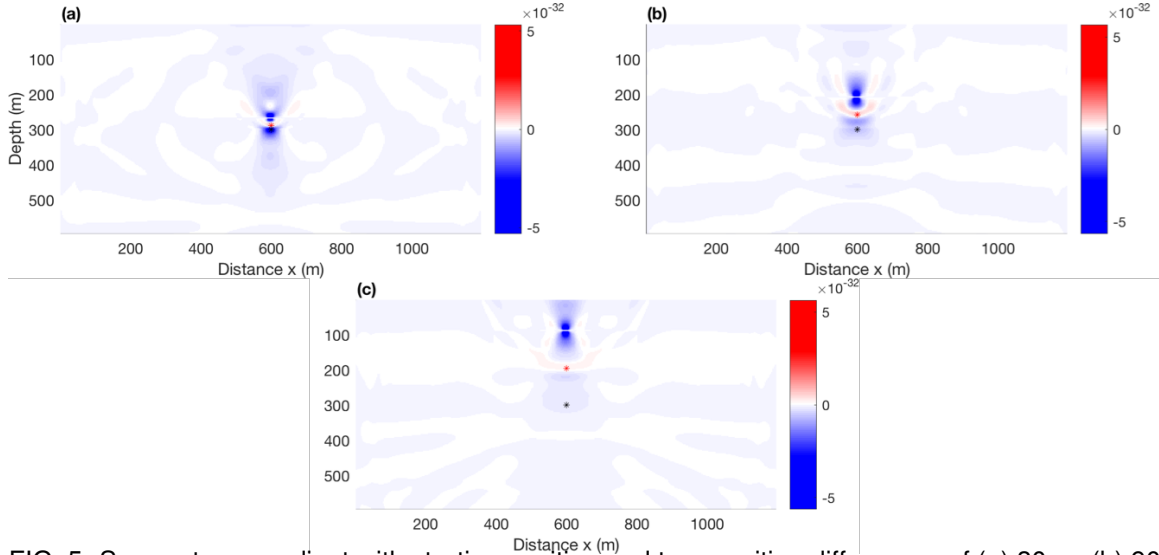


FIG. 5. Source-term gradient with starting position and true position differences of (a) 30 m, (b) 90 m and (c) 210 m after one iteration. Red stars indicate the position of the maximum of the gradient, which is taken as the next source position for the subsequent iteration. Black stars indicate the true source position, and are overlapping with the red stars in (a) and (b). The starting source position is at the center of each dark blue region.

Frequency

The next parameter worth testing is the frequency. Since microseismic events and earthquakes range in dominant frequency from tens to hundreds of Hz, it is important that the method be able to respond appropriately to the varied frequency content. Figure 6 shows the source-term gradient for a source separation of 90 m and a double couple moment tensor (Figure 5b), but for frequencies of 30 Hz, 60 Hz and 120 Hz.

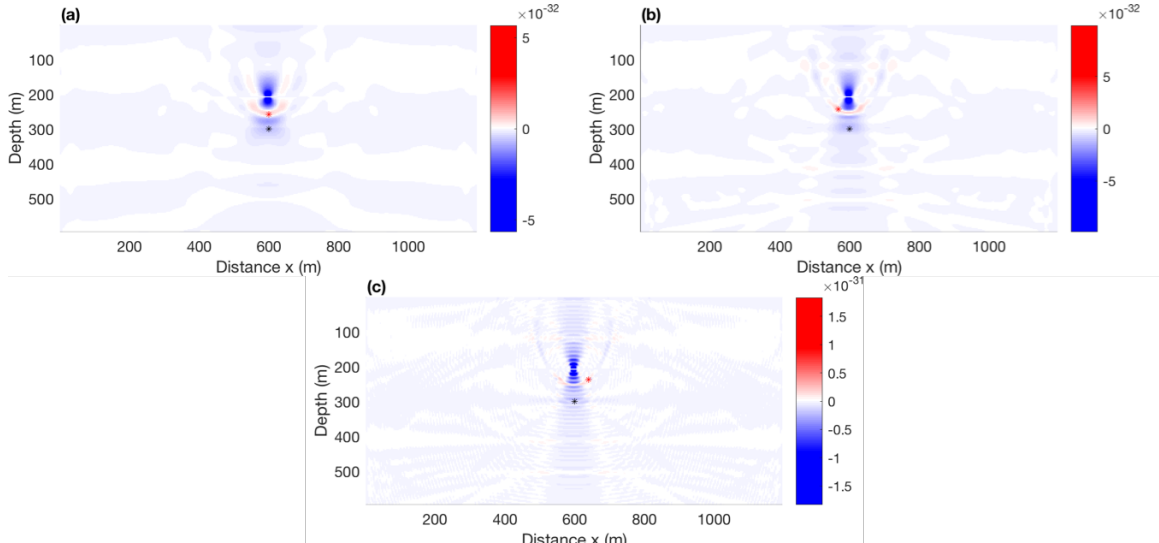


FIG. 6. Source-term gradient as a function of frequency with (a) 30 Hz, (b) 60 Hz and (c) 120 Hz after one iteration. Red stars indicate the maximum of the source-term gradient, and the black stars indicate the true source position. The starting source position is at the center of each dark blue region.

As frequency increases, artifacts on the sides of the positive region get larger, and so does the difference between the true position and next starting position determined by the gradi-

ent. In Figure 6c, there is a ‘ringing’ of the gradient, which is likely caused by dispersion. Taken together, these results are consistent with what was found in the acoustic case. Lower frequency sources are more stable in the inversion and therefore, higher magnitude microseismic and earthquake signals are more suitable for the application of this method.

Moment tensor

One advantage of having an elastic environment is the ability to define a moment tensor. A moment tensor is a 3 by 3 matrix that defines the radiation pattern of a source. An isotropic, explosive source, for example, is given by ones along the diagonal, and zeros in the remaining spaces. This produces a purely P-wave source. Commonly, sources studied in seismology are considered to be double-couple because shear slip is the main mechanism that occurs during earthquakes. A double-couple moment tensor is given by

$$M = \begin{bmatrix} 0 & 0 & 0 \\ 0 & -1 & 0 \\ 0 & 0 & 1 \end{bmatrix} . \quad (5)$$

Another type of source that is often discussed in the microseismic field is a Compensated Linear Vector Dipole (CLVD) source, which signifies tensile crack opening, and is commonly observed during hydraulic fracturing. This source has a moment tensor given by

$$M = \begin{bmatrix} 1 & 0 & 0 \\ 0 & 1 & 0 \\ 0 & 0 & -2 \end{bmatrix} . \quad (6)$$

To begin with, let’s assume that the moment tensor is known before the inversion, so both the observed data and modelled data are created with the true moment tensor. Figure 7 shows a comparison of the source-term gradient for the three different kinds of moment tensors discussed above (explosive, double couple and CLVD). A frequency of 60 Hz was used, with a separation distance of 90 m. Clearly, the moment tensor matters in the sense that it changes the shapes of the lobes of the gradient. However, in all three cases, the maximum of the gradient is in the right direction.

In practice, moment tensor inversion of often completed after events have been located, so it is not a safe assumption that the moment tensor would be known a priori. Therefore, in Figure 8 we show what the gradient looks like if we use a double couple or CLVD source to generate the observed data, and an explosive source to generate the modelled data. Although the shape of the gradient is different, and there is now a larger positive lobe for both cases, there is not much difference between the location of the maxima in this case and in the previous figure. Therefore, at least for this particular parameterization, the moment tensor does seem to be particularly important. It will remain to be seen if this is the case when dealing with real data.

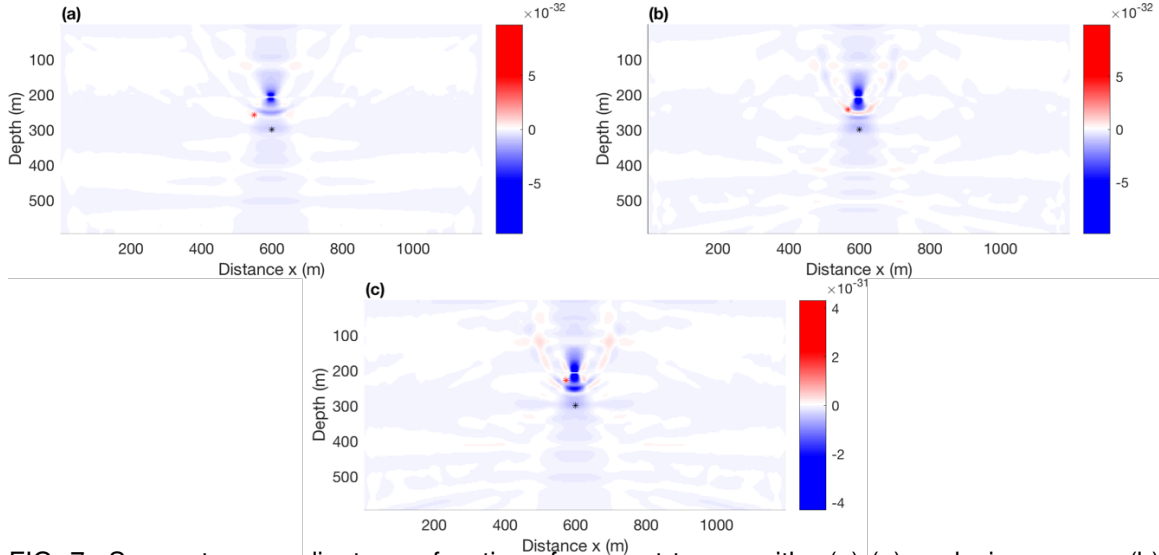


FIG. 7. Source-term gradient as a function of moment tensor with a(n) (a) explosive source, (b) double couple source, and (c) CLVD source after one iteration. Red stars indicate the maximum of the source-term gradient, and the black stars indicate the true source position. The starting source position is at the center of each dark blue region.

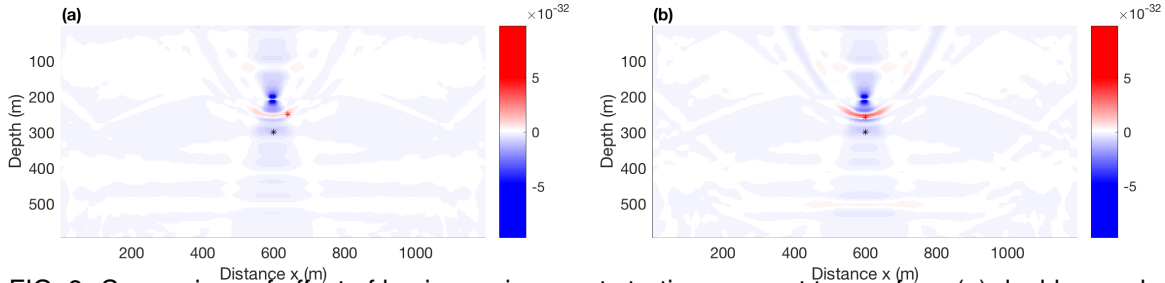


FIG. 8. Comparison of effect of having an incorrect starting moment tensor for a (a) double couple source and (b) CLVD source. Red stars indicate the maximum of the source-term gradient, and the black stars indicate the true source position. The starting source position is at the center of each dark blue region.

Realistic geometry

In all of the previous cases, we have assumed an environment where the wavefield is known at all positions. Though this environment was helpful to study the character of the source-term gradient, realistically, receivers are much more limited in space. Therefore, as a next step toward being able to apply this algorithm to real data, a realistic geometry needs to be tested. Of interest are two main configurations - receivers arrayed at the surface, and receivers in a borehole.

Based on the previous experiments, we choose a source separation of 90 m, a dominant frequency of 50 Hz, and a double couple moment tensor. Figure 9a shows the gradient, and it looks quite a bit different from the previous images, but still retains some basic characteristics. For one, there is still a region of negative values around the incorrect starting location, and there is a region of positive values in the direction of the true location, but it is too deep, and is less focused than before. Considering that we are now using but a fraction of the wavefield compared to before, it is not entirely unexpected.

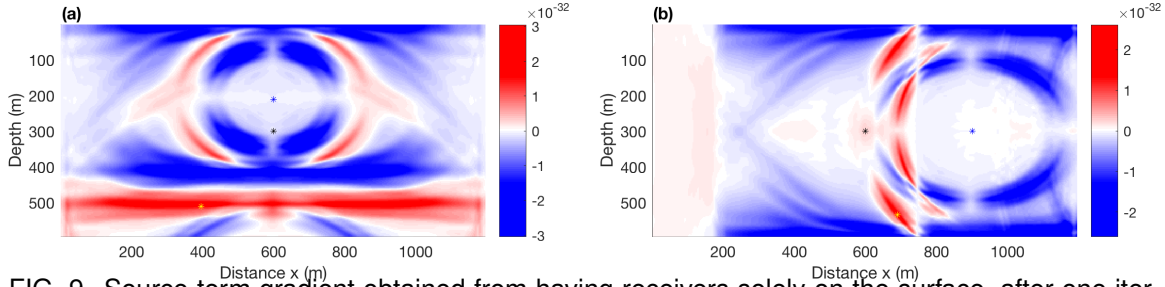


FIG. 9. Source-term gradient obtained from having receivers solely on the surface, after one iteration. Yellow stars indicate the maximum of the source-term gradient, and the black stars indicate the true source position. The starting source position is shown as a blue star.

Figure 9b shows the gradient in the case that there is a 300 m lateral separation of the starting position and true position. Promisingly, there is a consistent type of behaviour, and there is again a positive region in the direction of the true position. Indeed, these examples show that despite having receivers only on the surface, the gradient still retains sensitivity to position both laterally and vertically.

There are a few implications for applications to real data that arise from these results. For one, it is likely that a regularization would have to be applied to the gradient in order to obtain a more reasonable next starting position for the subsequent iteration. In the above examples, it would have to return a starting position somewhere in between the positive regions, and the starting position.

Another common geometry is to have receivers arrayed vertically in a borehole. For simplicity, let's assume that we have receivers from the surface down to the bottom of the model space. Figure 10 shows the gradient for such an arrangement, with (a) for a vertical positioning error, and (b) for a lateral positioning error. The results appear to be quite different from the surface case, and it is difficult to infer what direction the gradient should be operating in. Therefore, it appears that surface geometries are more suited for the application of MFWI. Of course, further work is required to investigate causes and perhaps remedies to this conclusion.

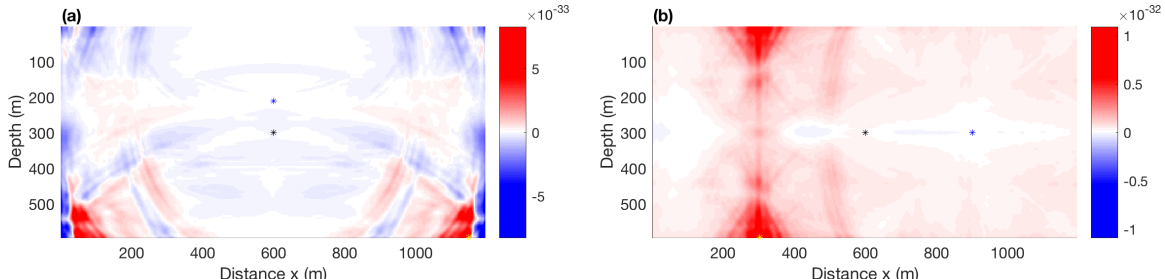


FIG. 10. Source-term gradient obtained from having receivers vertically along the right boundary of the model, after one iteration. Yellow stars indicate the maximum of the source-term gradient, and the black stars indicate the true source position. The starting source position is shown as a blue star.

Cross talk

The final parameter to explore is the background velocity model. The previous sections all have a homogeneous velocity model that is the same for the observed and modelled data. This is another unrealistic expectation and it is not difficult to see that having an

incorrect velocity model would change the position of the inverted source location. To test this quantitatively, we devise two experiments. The first experiment is to keep a homogeneous background medium, but change the S-wave velocity of the starting model. In some practical applications, well-log data may be sparse, and only sonic logs may be available. In that case, the S-wave velocity model is often reconstructed from the sonic log by assuming a V_P/V_S ratio. If this ratio is incorrect, then we get the problem that is being tested in this model – a correct P-wave model, but an incorrect S-wave model.

Figure 11 shows the results of overestimating the S-wave velocity by 200 m/s and underestimating the S-wave velocity model by 150 m/s. In the true model, $V_P/V_S = 1.5$, whereas these added errors result in V_P/V_S ratios of 1.36 and 1.62, respectively. These are of course relatively small errors, but they convey the proper concept. In this case, underestimating the S-wave velocity appears to cause more damage to the gradient than overestimating it.

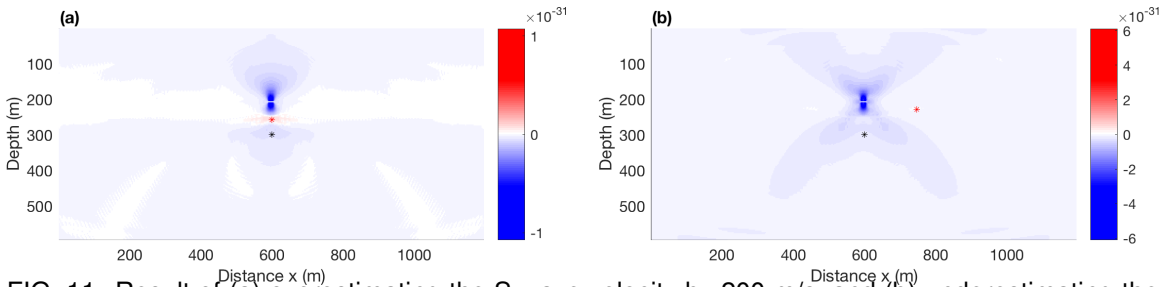


FIG. 11. Result of (a) overestimating the S-wave velocity by 200 m/s, and (b) underestimating the S-wave velocity by 150 m/s. Red stars indicate the maximum of the source-term gradient, and the black stars indicate the true source position. The starting source position is at the center of each dark blue region.

The second test involves adding variable velocity to the model. Consider a P-wave velocity gradient from 2800 m/s to 3100 m/s over 600 m, and a constant V_P/V_S ratio of 1.5. This would be like a part of a layered basin where velocity normally increases with depth. Consider next that there is a basement layer at 360 m below the surface with a velocity of 3400 m/s. In this miniature basin suppose there were no well logs that went below 360 m, so a constant gradient was assumed for the starting model. Figure 12 shows the P-wave velocity model, as well as the gradient for the case where the starting model failed to account for the faster basement velocity. We can see that the maximum of the gradient is no longer in the direction of the true source location. The shape, however, is the same, suggesting that some form of regularization for the gradient could allow for a recovery of the source direction relative to the starting point. Once a robust regularization scheme is established, more meaningful tests can be conducted to further study the effect of the cross-talk between the two main parameters.

These simple examples serve to show the importance of the second half of the elastic MFWI formulation, which are simultaneous updates to the velocity model. Although this can be a powerful method to locate microseismic events or other subsurface sources, the real utility and innovation of this method is its ability to simultaneously correct the velocity model. However, the implementation of the full method is out of the scope of this report.

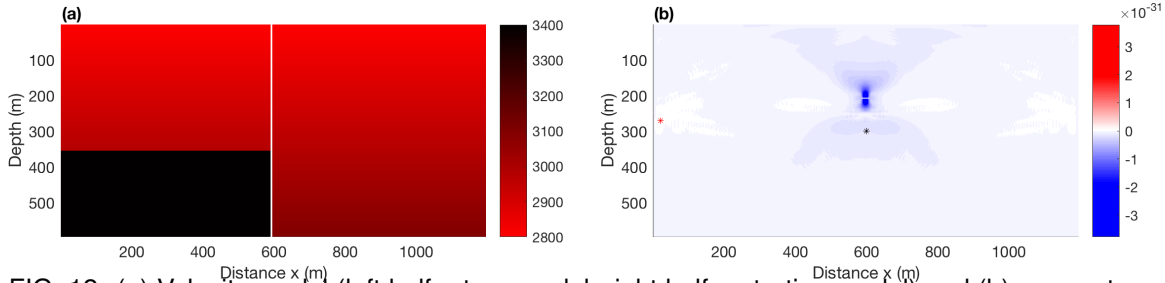


FIG. 12. (a) Velocity model (left half = true model, right half = starting model) and (b) source-term gradient for a true model with the higher velocity basement, but a starting model without it. Red stars indicate the maximum of the source-term gradient, and the black stars indicate the true source position. The starting source position is at the center of each dark blue region.

APPLICATION TO REAL DATA

Any theory is only useful if it can be applied. To that end, the ultimate goal of MFWI is to apply it to real data in order to locate microseismic events. In this section, we propose a dataset to which elastic MFWI can be applied. This is a downhole microseismic dataset from the Horn River Basin in British Columbia. The velocity model and acquisition geometry are shown in Figure 13. There are twelve 3C geophones recording a hydraulic fracturing operation.

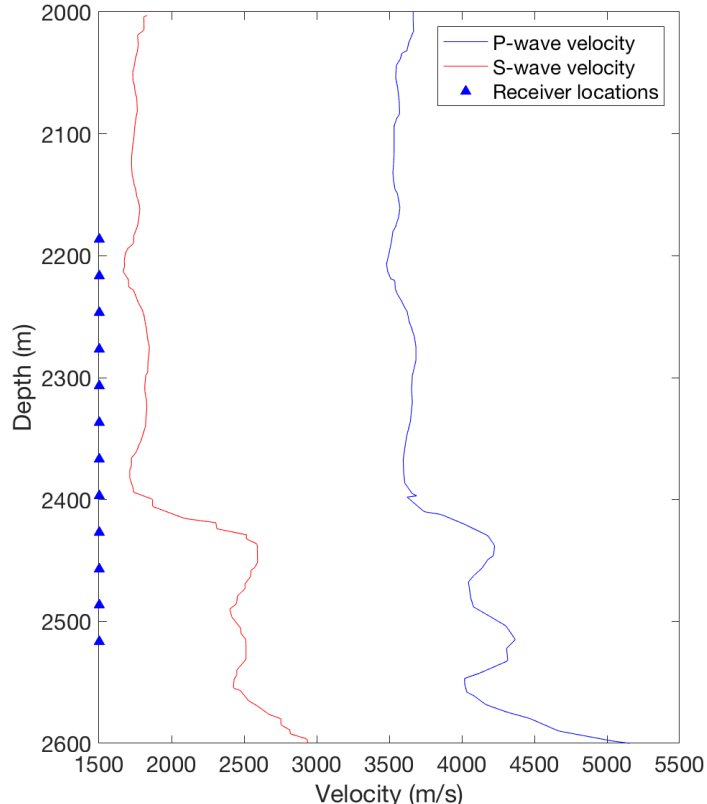


FIG. 13. Velocity model and downhole acquisition geometry for the Horn River dataset.

This dataset was chosen because the microseismic events are on the order of a few hundred meters away from the receivers, and the velocity model is well constrained. Additionally, due to the geometry, the situation may be treated in 2D, which makes it simpler to apply. Figure 14 shows a comparison of the finite difference waveforms and the real event

waveforms. In this example we see the limitations of the particular finite difference code used. Due to the using of lower order finite difference approximations, a non-staggered grid, and very simple boundary conditions, the modelled waveforms are not a perfect reconstruction. Also, the frequency content in the modelled trace is too low. Another point to consider is anisotropy. In the real waveforms, there is clear evidence of shear-wave splitting, which due to the 2D nature of the modelling, is uncaptured. This is likely to create difficulty for the calculation of the source-term gradient.

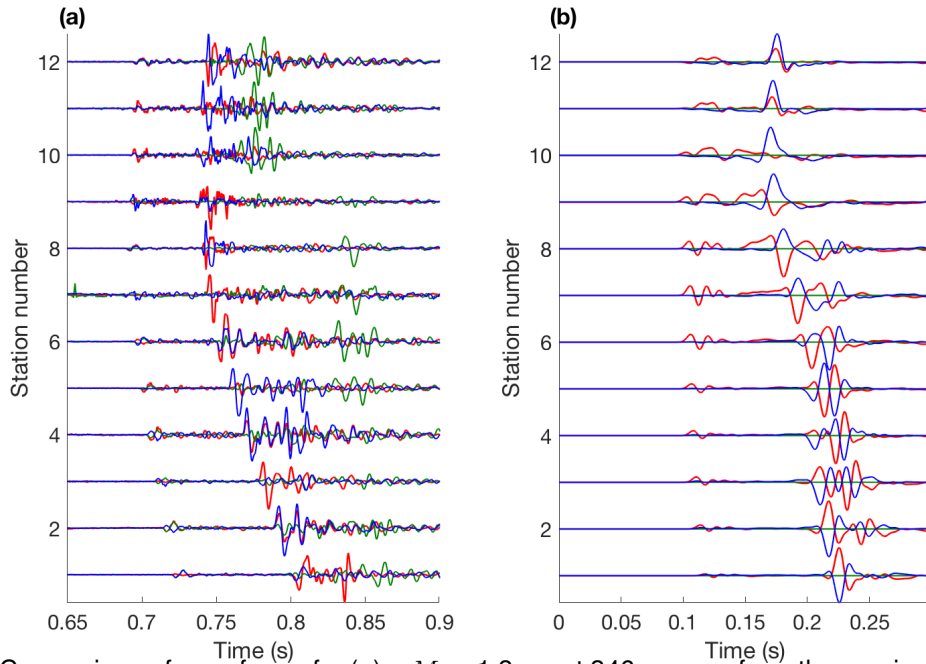


FIG. 14. Comparison of waveforms for (a) a M_W -1.3 event 346 m away from the receiver well, and (b) the finite difference modelled waveforms of an event at the same position.

DISCUSSION AND FUTURE WORK

There is much that remains to be explored with elastic MFWI. The approach here only focused on inverting for source location, but if re-parameterized, several other useful source characteristics could be determined. Among them, one option is to allow for the inversion of the moment tensor. One reason this may not be necessary is that in the microseismic field there exist a multitude of efficient and robust methods to invert for the moment tensor. Also, it is often not necessary to obtain a moment tensor for every single event, but rather, it is more useful to have all possible locations, and a handful of representative moment tensors. Another parameter that could be inverted for is the origin time (t^* in equation 3). However, this is also not a particularly useful parameter since it is often not required for many processing applications.

One practical change that is necessary is to change to a more robust finite difference modelling code. This would allow for more accurate reconstructions of the wavefields, and allow the investigation of behaviour at both lower and higher frequencies. Additionally, the results presented herein were limited to the source-term gradient, and as such, were only half of the proposed implementation. Future work would involve having both the velocity model gradient and source term gradient solved simultaneously. The most useful potential outcome of this work would be to develop a robust, and field-data-tested method able to

survive the pitfalls of having an erroneous starting velocity model.

The ultimate goal of FWI is to be applied to real data. In the very early work shown with real data, there remains a lot to be done. Exploring how different components of the wavefield (x , y , and z) construct the gradient will be interesting, as well as testing many different kinds of preconditioning and regularization strategies. In terms of preconditioning, one possible direction would be to look at how different filters effect the results, and whether a multiscale frequency approach (from low to high frequency) would allow for higher location resolution.

CONCLUSIONS

The early stages of elastic microseismic full waveform inversion were presented. The behaviour of the gradient is consistent with what was observed in the acoustic implementation, with the addition of increased complexity due to having a moment tensor. Separation distances on the order of a few hundred meters between the starting position and true position were shown to be acceptable, and lower frequency data yielded better results. Although the algorithm does not seem to be sensitive to the moment tensor, further work is required in regards to testing parameterizations that have the moment tensor inherently within them. The largest limiting factor for FWI appears to be the geometry, although cross talk with the velocity model can also introduce significant errors. Future work involves making the gradient more robust in these circumstances, and moving toward a real data application.

ACKNOWLEDGEMENTS

The authors thank the sponsors of CREWES for continued support. This work was funded by CREWES industrial sponsors and NSERC (Natural Science and Engineering Research Council of Canada) through the grant CRDPJ 461179-13. We also thank the sponsors of the Microseismic Industry Consortium for providing the data. Nadine Igonin is also funded through the NSERC PGS-D and SEG Earl D. and Reba C Griffin Memorial Scholarship.

REFERENCES

- Boyd, O., 2006, An efficient Matlab script to calculate heterogeneous anisotropically elastic wave propagation in three dimensions: *Computers & Geosciences*, **32**, 259–264.
- Igonin, N., and Innanen, K., 2017a, Applications of FWI to the microseismic source problem: CREWES Research Report, **29**.
- Igonin, N., and Innanen, K., 2017b, Toward full waveform inversion for source location and velocity model: gradient and Hessian: CREWES Research Report, **29**.
- Keating, S., and Innanen, K., 2018, Viscoelastic FWI: solving for QP, QS, VP, VS and density: CREWES Research Report, **30**.
- Pan, W., 2018, Elastic full-waveform inversion and parametrization analysis applied to walk-away vertical seismic profile data for unconventional (heavy oil) reservoir characterization: *Geophysics Journal International*, **213**, 1934–1968.
- Rashedi, H., 2015, Finite-difference simulation of synthetic microseismograms: M.Sc. thesis, Univ. of Calgary.

- Tan, Y., He, C., and Mao, Z., 2018, Microseismic velocity model inversion and source location: The use of neighborhood algorithm and master station method: *Geophysics*, **83**, No. 4, KS49–KS63.
- Tarantola, A., 1984, Inversion of seismic reflection data in the acoustic approximation: *Geophysics*, **49**, No. 8, 1259–1266.
- Wang, H., and Alkhalifah, T., 2018, Microseismic imaging using a source function independent full waveform inversion method: *Geophysics Journal International*, **214**, 46–57.
- Zhang, Z., Du, J., and Gao, F., 2018, Simultaneous inversion for microseismic event location and velocity model in Vaca Muerta Formation: *Geophysics*, **83**, No. 3, KS23–KS34.